

# Naval Research Laboratory

Washington, DC 20375-5320



NRL/FR/7230--04-10,060

## PHILLS-1 Hyperspectral Data Processing: 2001 LEO-15 Deployment

WILLIAM A. SNYDER

CURTISS O. DAVIS

JEFFREY H. BOWLES

WEI CHEN

BO-CAI GAO

DAVID GILLIS

DANIEL KORWAN

GIA LAMELA

MARCOS MONTES

W. JOSEPH RHEA

*Coastal and Optical Experiments Section  
Coastal and Ocean Remote Sensing Branch  
Remote Sensing Division*

May 26, 2004

# REPORT DOCUMENTATION PAGE

Form Approved  
OMB No. 0704-0188

Public reporting burden for this collection of information is estimated to average 1 hour per response, including the time for reviewing instructions, searching existing data sources, gathering and maintaining the data needed, and completing and reviewing this collection of information. Send comments regarding this burden estimate or any other aspect of this collection of information, including suggestions for reducing this burden to Department of Defense, Washington Headquarters Services, Directorate for Information Operations and Reports (0704-0188), 1215 Jefferson Davis Highway, Suite 1204, Arlington, VA 22202-4302. Respondents should be aware that notwithstanding any other provision of law, no person shall be subject to any penalty for failing to comply with a collection of information if it does not display a currently valid OMB control number. PLEASE DO NOT RETURN YOUR FORM TO THE ABOVE ADDRESS.

1. REPORT DATE (DD-MM-YYYY) May 26, 2004			2. REPORT TYPE NRL Formal Report		3. DATES COVERED (From - To)	
4. TITLE AND SUBTITLE  PHILLS-1 Hyperspectral Data Processing: 2001 LEO-15 Deployment					5a. CONTRACT NUMBER	
					5b. GRANT NUMBER	
					5c. PROGRAM ELEMENT NUMBER	
6. AUTHOR(S)  W.A. Snyder, C.O. Davis, J.H. Bowles, W. Chen, B. Gao, D. Gillis, D. Korwan, G. Lamela, M. Montes, and W.J. Rhea					5d. PROJECT NUMBER	
					5e. TASK NUMBER	
					5f. WORK UNIT NUMBER	
7. PERFORMING ORGANIZATION NAME(S) AND ADDRESS(ES)  Naval Research Laboratory 4555 Overlook Avenue, SW Washington, DC 20375-5320					8. PERFORMING ORGANIZATION REPORT NUMBER  NRL/FR/7230--04-10,060	
9. SPONSORING / MONITORING AGENCY NAME(S) AND ADDRESS(ES)  Office of Naval Research 800 North Quincy Street Arlington, VA 22217-5660					10. SPONSOR / MONITOR'S ACRONYM(S)  ONR	
					11. SPONSOR / MONITOR'S REPORT NUMBER(S)	
12. DISTRIBUTION / AVAILABILITY STATEMENT  Approved for public release; distribution is unlimited.						
13. SUPPLEMENTARY NOTES						
14. ABSTRACT  The Portable Hyperspectral Imager for Low-Light Spectroscopy (PHILLS) is a hyperspectral imager specifically designed for imaging the coastal ocean. It was deployed at LEO-15 during July 22 through August 2, 2001. This report describes the LEO-15 2001 PHILLS-1 data that were collected and how they were processed to obtain calibrated and atmospherically corrected remote sensing reflectance images. This includes descriptions of laboratory spectral and radiance calibration procedures, how laboratory calibrations are adjusted to match field-collected data, and how the data can then be atmospherically corrected and georectified.						
15. SUBJECT TERMS  Hyperspectral, Remote sensing						
16. SECURITY CLASSIFICATION OF:  a. REPORT Unclassified			17. LIMITATION OF ABSTRACT  UL	18. NUMBER OF PAGES  29	19a. NAME OF RESPONSIBLE PERSON William Snyder	
b. ABSTRACT Unclassified					19b. TELEPHONE NUMBER (include area code) 202-404-1376	
c. THIS PAGE Unclassified						

## CONTENTS

1. INTRODUCTION .....	1
2. LEO-15 PHILLS-1 2001 DATA SET .....	1
3. PREFLIGHT WAVELENGTH CALIBRATION .....	7
4. PREFLIGHT RADIOMETRIC CALIBRATION .....	7
5. CORRECTION OF SENSOR COUNTS FOR FRAME TRANSFER .....	11
6. ADJUSTMENT OF LABORATORY CALIBRATIONS TO MATCH FIELD DATA .....	13
7. SCATTERED LIGHT NEAR BRIGHT LAND FEATURES .....	15
8. DATA GEOREFERENCING .....	15
9. CALIBRATED PRODUCTS .....	19
10. ATMOSPHERIC CORRECTION OF THE DATA .....	20
11. ACKNOWLEDGMENTS .....	25
REFERENCES .....	25

## **PHILLS-1 HYPERSPECTRAL DATA PROCESSING: LEO-15 JULY 2001 DEPLOYMENT**

### **1. INTRODUCTION**

The Portable Hyperspectral Imager for Low-Light Spectroscopy (PHILLS) is a hyperspectral imager specifically designed for imaging the coastal ocean. It was deployed on an Antonov AN-2 aircraft operated by Bosch Aerospace, Inc. (Huntsville, Alabama) at the Long-term Ecosystem Observatory (LEO-15) during July 22 through August 2, 2001. The deployment was part of a multi-institution oceanographic study of the region sponsored by the U.S. Office of Naval Research (ONR) Hyperspectral Coupled Ocean Dynamics Experiments (HyCODE) program [1]. The goal of this program is to demonstrate the scientific and technical capability to characterize the littoral environment with remote sensors.

The LEO-15 site [2] is one of three regions studied by the HyCODE program. The study area is an approximate 25 km  $\times$  25 km area located in the Middle Atlantic Bight off the coast of New Jersey north of Atlantic City. Understanding how variability in the inherent optical properties of these waters is related to physical and biological processes is an important part of the HyCODE program. During the summer months, this area is the site of numerous in-water studies with instruments on fixed moorings, manned research vessels, and autonomous underwater vehicles. During the 2001 July deployment, this area was also observed with numerous aircraft and satellite multi- and hyperspectral visible/near-IR sensors, such as SeaWiFS, MODIS, AVIRIS, PHILLS-1, PHILLS-2, IKONOS, and PROBE.

The PHILLS sensors have been deployed during a number of field campaigns. In general, each deployment includes sensor improvements, although occasionally new sensors are constructed (e.g., the PHILLS-2 sensor also flew at LEO-15 [3]). The sensor described here was flown the previous year at LEO-15 and at Lee Stocking Island [4]. Because of sensor modifications, the light-scattering problems noted in those deployments are not present in this data set.

This report describes the LEO-15 2001 PHILLS-1 data that were collected and how they were processed to obtain calibrated and atmospherically corrected remote sensing reflectance ( $R_{rs}$ ) images. This includes descriptions of laboratory spectral and radiance calibration procedures, how laboratory calibrations are adjusted to match field-collected data, and how the data can then be atmospherically corrected and georectified.

### **2. LEO-15 PHILLS-1 2001 DATA SET**

While the main focus of the 2001 July field campaign was the 625 km<sup>2</sup> area located off the coast, the inshore areas (Great Bay, Barnegat Bay, and associated marshes) are also of great interest for estuarine studies. Consequently, our observation plan was constructed to observe not only the offshore area, but also to cover as much of the marsh and estuarine environment as possible.

PHILLS-1 is a pushbroom sensor. It views the Earth from the aircraft nadir position, with the spectrometer slit aligned perpendicular to the aircraft direction of motion. The aircraft's forward motion is used to sequentially acquire new lines of ground pixels in the along-track direction. The light passing through the

entrance slit is dispersed by the spectrograph onto a two-dimensional charge-coupled device (CCD) detector array to obtain a spectrum for each cross-track ground pixel. References 5 and 6 provide a detailed sensor description.

The PHILLS-1 sensor CCD has 1024 cross-track spatial pixels (or samples). The CCD spectral dimension is 512 pixels (or bands). The CCD is sensitive to light in the 400 to 1000 nm spectral range; consequently, at this maximum spectral resolution, each band has a width of  $\sim$ 1.17 nm. This maximal spectral resolution is used for laboratory sensor wavelength calibrations (see Section 3). Because of signal-to-noise and data volume considerations, however, field data are usually spectrally summed (binned on the CCD chip) over 4 or 8 bands, producing 128 or 64 spectral bands per spatial pixel. A sensor frame is one line of data. In the laboratory, where the sensor is not moving, measurements taken over many frames represent a measurement over time, which is usually then averaged over time (frames) to produce a 1024 across-track pixel by 512, 128, or 64 spectral band data matrix, depending upon the spectral binning. When flown in an aircraft, each frame covers a different cross-track line on the ground, and the result is a 1024 sample  $\times$  (128 or 64 band)  $\times$  (# of lines) data cube in Band Interleaved by Line (BIL) format. Generally the data are stored in separate “sequences” containing 1024 lines, which, when strung together, form a data “run.”

The LEO-15 data were collected using a 17 mm lens at f/4 and focused at infinity. The altitude of the plane/sensor was  $\sim$  2700 m for those flights covering the offshore area. The camera frame rate was 25 frames/s in order to produce 1.8 m square pixels, and 128 bands of spectral data per spatial pixel (bin-by-4) were saved. For flights on July 27 and August 2, we surveyed the inland marsh area at higher (0.9 m) spatial resolution at a flight altitude of 1500 m. This required setting the sensor frame rate to 46 frames/s in order to maintain square spatial pixels. In this case, data were stored at 64 bands per spatial pixel (bin-by-8). Binned-by-4 PHILLS-1 data exhibit a small band-to-band sawtoothed pattern that is not removed by the radiometric calibration. It is believed that this pattern is at least partially due to an etalon effect within the CCD. Summing adjacent bands to produce 64 spectral bands per pixel can significantly reduce this effect, and as a consequence, all LEO-15 calibrated PHILLS-1 data are routinely binned to 64 wavelength bands. The original bin-by-4 spectral data are available for special studies if needed.

Remote sensing data were collected on 9 days at LEO-15 with PHILLS-1. Figure 1 shows a schematic of each flight line on a map of the region. Flight lines are aligned along the mean solar azimuthal angle. The approximate start/stop time, latitude, and longitude of each run is listed in Table 1. Data are stored in sequences of 1024 lines (frames) of data. Each flight line is given a run number and each data sequence is named according to that run number and the sequence number within that run, i.e., RunXXSeqYY.bil. Calibrated data are normally identified with a date identifier and calibration ID (e.g., YYMMDD\_RunXXSeqYY\_calID.bil). Associated with each data file is an ASCII header file (\*.hdr) in ENVI format [7] that contains information about the file. One can identify data of interest by downloading the appropriate “quick look” RGB image of the run from the NRL Code 7230 website [8] and identifying the lines of interest. The sequence number for those lines is the truncated integer of (line number)/1024. Each data run has an associated “dark file” of at least one sequence in length that was usually made at the end of the run by placing the sensor lens cap over the lens. This dark file must be subtracted from a data sequence before that sequence can be calibrated.

Of the nine flight days, the prime science days were July 23, 25, 27, 31 and August 1 and 2, 2001. The high 0.9 m spatial resolution marsh and estuary survey occurred on July 27 and August 2. The spatial resolution was 1.8 m for the other flights and the flight lines coincide with the PHILLS-2 sensor flight lines on those days. The data collection on August 1 is somewhat different in that a time series was run repeatedly on two lines. The July 31 observation is especially noteworthy because of the many near-simultaneous remote sensing plane and satellite systems that observed this region on that day.

In addition to the aircraft data discussed in this report, our group also collected in-water ground-truth data for comparison and interpretation of remote sensing-derived reflectance spectra. Water samples were collected for filter pad absorption measurements, total suspended sediment, particle size and chemical composition (HPLC). An optical profiler containing two AC9s, a HiSTAR, and a Hydroscat-6 instrument were also used. An Analytical Spectral Devices (ASD) spectrometer was used for measuring  $R_{rs}$  at the water surface. A complete description of the ground truth measurements, data processing, and data products can be found in Ref. 9. The date, time, location, and data available are listed in Table 2. Additional extensive ship and mooring data were collected by other HyCODE participants. The HyCODE website [1] provides information and links to other sites regarding these measurements.

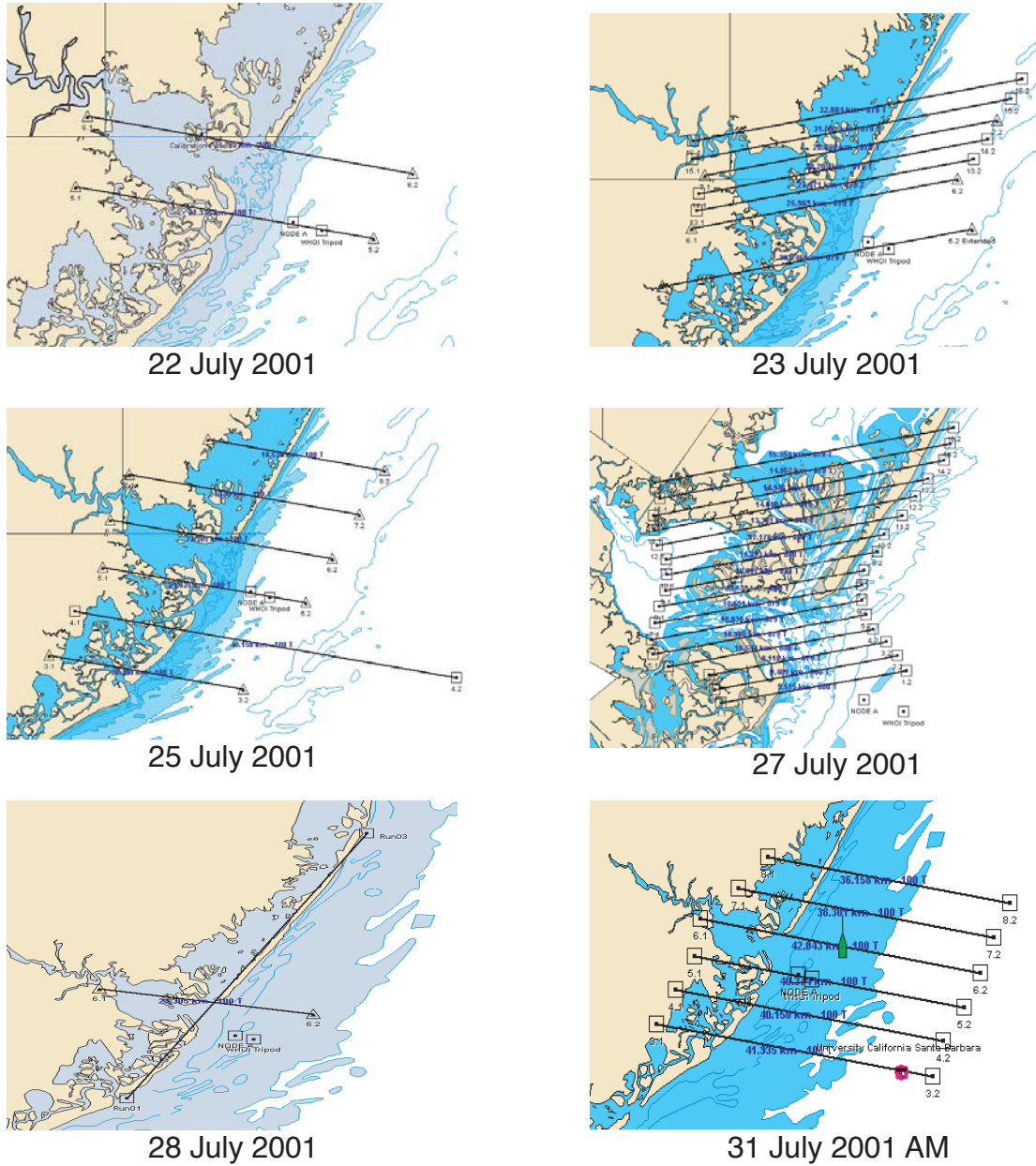


Fig. 1 — A schematic of the flight lines at LEO-15. The orientation of the lines is aligned with the local solar azimuth angle at the time of the flight. The cross-track field of view is given approximately by the separation of the lines on July 23, 2001 for July 22, 23, 25, 28, and 31 AM and PM and August 1, and by the separation of the lines on July 27 for the flight on that day and August 2.

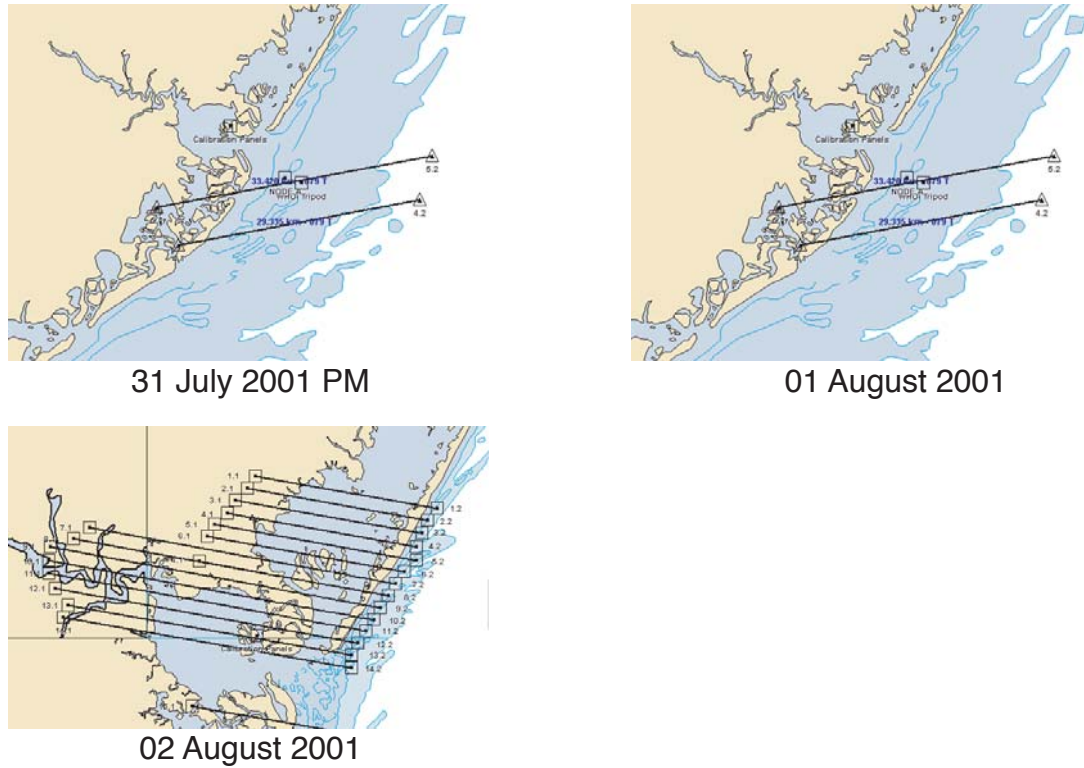


Fig. 1 (continued) — A schematic of the flight lines at LEO-15. The orientation of the lines is aligned with the local solar azimuth angle at the time of the flight. The cross-track field of view is given approximately by the separation of the lines on July 23, 2001 for July 22, 23, 25, 28, and 31 AM and PM and August 1, and by the separation of the lines on July 27 for the flight on that day and August 2.

Table 1 — LEO-15 Data Runs: July 22 – August 2, 2001

Run	Start					Altitude (m)	Stop					Altitude (m)
	GMT Hour	Minute	Latitude	Longitude			Hour	Minute	Latitude	Longitude		
22 July												
	3	13	32.795	39	29.517	-74	9.452	2608		13	40.360	39
	5	13	42.268	39	29.354	-74	26.806	2587		13	50.394	39
	9	13	53.766	39	29.490	-74	9.461	2620		14	1.068	39
	12	14	10.004	39	29.136	-74	26.492	1499		14	16.973	39
	14	14	20.030	39	29.496	-74	9.471	1500		14	27.751	39
	17	14	31.749	39	29.544	-74	27.564	1510		14	38.980	39
	19	14	42.910	39	29.705	-74	10.162	1518		14	50.236	39
23 July												
	1	19	26.549	39	31.750	-74	10.905	2648		19	34.645	39
	4											
	6	19	55.897	39	28.817	-74	7.545	2656		20	7.012	39
	8											
	10,11	20	25.039	39	35.279	-74	5.778	2636		20	36.507	39
	13	20	37.822	39	33.017	-74	27.010	2670		20	49.022	39
	16	20	51.817	39	34.147	-74	6.387	2685		21	2.467	39
	20	21	8.973	39	25.903	-74	30.194	2708		21	20.307	39
	22	21	24.069	39	31.102	-74	9.291	2660		21	33.095	39
25 July												
	0	12	44.463	39	22.229	-74	15.727	2691		12	52.228	39
	2	13	0.047	39	35.978	-74	19.948	2685		13	7.708	39
	4	13	10.593	39	32.231	-74	7.106	2691		13	20.192	39
	6	13	22.378	39	32.014	-74	26.053	2693		13	30.455	39
	8	13	39.090	39	22.902	-74	0.414	2671		13	53.298	39
	10	13	55.360	39	28.984	-74	26.466	2708		14	9.563	39
	12	14	12.872	39	22.745	-73	59.781	2690		14	27.945	39

Table 1 (continued) — LEO-15 Data Runs: July 22 – August 2, 2001

Run	GMT			Start			Altitude (m)	Stop			Altitude (m)
	Hour	Minute	Latitude	Longitude				Hour	Minute	Latitude	
<b>27 July</b>											
0	19	20.327	39 33.635	-74 23.358	1498		19	26.566	39 35.290	-74 12.183	1499
2	19	28.904	39 34.748	-74 12.763	1501		19	33.606	39 33.223	-74 23.206	1504
4	19	36.631	39 32.720	-74 23.740	1497		19	43.376	39 34.378	-74 12.625	1517
6	19	45.292	39 33.897	-74 13.370	1529		19	50.019	39 32.297	-74 23.499	1525
8	19	52.867	39 31.987	-74 23.087	1548		19	57.350	39 33.319	-74 13.855	1531
10	20	1.742	39 32.783	-74 14.281	1525		20	6.314	39 31.517	-74 22.960	1546
12	20	8.507	39 31.116	-74 22.906	1528		20	13.216	39 32.334	-74 14.722	1548
14	20	14.829	39 31.780	-74 15.046	1550		20	18.906	39 30.688	-74 23.057	1558
16	20	20.666	39 30.243	-74 23.284	1541		20	25.049	39 31.315	-74 15.401	1567
18	20	26.922	39 30.759	-74 15.833	1519		20	30.767	39 29.755	-74 23.340	1571
20	20	32.559	39 29.331	-74 23.387	1546		20	36.749	39 30.530	-74 15.514	1531
22	20	38.550	39 29.883	-74 16.223	1500		20	41.967	39 29.034	-74 22.709	1551
25	20	44.747	39 28.524	-74 22.839	1538		20	48.804	39 29.679	-74 15.164	1520
27	20	50.766	39 29.363	-74 14.861	1533		20	54.236	39 28.366	-74 21.576	1563
29	20	55.991	39 27.993	-74 21.303	1529		20	59.631	39 28.988	-74 14.224	1520
31	21	1.296	39 28.545	-74 14.154	1525		21	4.922	39 27.531	-74 21.274	1517
<b>28 July</b>											
1	12	49.517	39 20.947	-74 25.206	2607		13	6.583	39 43.286	-74 6.827	2615
4	13	9.650	39 44.105	-74 6.231	2630		13	25.817	39 22.186	-74 24.107	2613
6	13	38.310	39 28.833	-74 6.329	2617		13	48.114	39 31.796	-74 26.197	2598
<b>31 July (am)</b>											
3	12	27.600	39 24.142	-74 30.517	2625		12	41.670	39 20.318	-74 3.013	2613
5	12	46.033	39 22.716	-74 0.892	2620		12	59.417	39 26.524	-74 27.461	2618
7	13	8.900	39 36.321	-74 20.089	2610		13	20.967	39 33.108	73 55.103	2608
9	13	24.100	39 30.614	-73 55.314	2607		13	35.883	39 33.426	-74 18.426	2614
11	13	41.333	39 28.518	-74 23.286	2612		13	53.200	39 25.580	73 59.705	2619
13	14	0.900	39 25.739	-74 1.963	2584		14	7.817	39 27.604	-74 15.449	2525
15	14	16.533	39 31.600	-74 25.936	2627		14	30.600	39 28.009	-73 57.700	2633
<b>31 July (pm)</b>											
2	19	25.340	39 30.451	-74 25.779	2611		19	38.225	39 34.163	-74 0.064	2620
<b>1 August</b>											
2	20	17.190	39 26.181	-74 24.277	2675		20	27.450	39 29.016	-74 4.309	2660
4	20	29.932	39 26.181	-74 5.199	2634		20	39.378	39 23.314	-74 24.567	2624
6	20	43.863	39 26.261	-74 23.690	2639		20	53.361	39 28.877	-74 4.704	2631
8	20	55.608	39 26.106	-74 5.663	2643		21	5.215	39 23.429	-74 24.743	2642
10	21	8.591	39 26.277	-74 23.134	2655		21	18.261	39 28.985	-74 4.550	2642
12	21	20.743	39 26.236	-74 4.826	2655		21	31.148	39 23.287	-74 25.476	2657
<b>2 August</b>											
2	12	29.939	39 35.349	-74 12.409	1562		12	34.199	39 36.475	-74 20.668	1529
4	12	35.990	39 36.073	-74 20.906	1520		12	40.194	39 34.867	-74 12.489	1502
6	12	43.047	39 34.503	-74 13.096	1533		12	47.689	39 35.694	-74 21.625	1538
8	12	49.532	39 35.163	-74 21.359	1546		12	53.629	39 34.020	-74 13.234	1552
10	12	56.907	39 33.571	-74 13.389	1559		13	1.515	39 34.818	-74 22.136	1531
12	13	3.380	39 34.351	-74 22.214	1542		13	7.725	39 33.176	-74 13.694	1542
14	13	10.489	39 32.814	-74 14.338	1547		13	17.464	39 34.711	-74 27.578	1544
16	13	21.149	39 34.328	-74 27.901	1534		13	28.205	39 32.388	-74 14.497	1539
19	13	34.857	39 32.042	-74 15.046	1521		13	42.117	39 34.070	-74 29.238	1574
21	13	44.712	39 33.464	-74 28.526	1573		13	51.397	39 31.635	-74 15.045	1532
23	13	53.804	39 31.269	-74 15.614	1531		14	0.842	39 33.163	-74 29.344	1576
25	14	3.510	39 32.632	-74 28.851	1561		14	10.192	39 30.810	-74 15.755	1534
27	14	12.647	39 30.535	-74 16.730	1538		14	18.624	39 32.145	-74 28.632	1550
29	14	21.174	39 31.704	-74 28.442	1561		14	27.484	39 30.011	-74 16.014	1564
31	14	31.122	39 27.499	-74 13.623	1559		14	35.939	39 28.779	-74 23.234	1551

Table 2 – Master NRL Inwater Data Log for LEO-15 2001

Updated 12/04/2002

Date	Local Time	Station Time, Location, and Name				Optics Profile	Rrs	Sun Photometer	Pad Absorption	CDOM	[chl a]	HPLC	TSS/LPC	Data collected at Station	
		GMT	Lat_deg	Lat_min	Lon_deg										
July 21, 2001	14:30	18:30	39	27.5834	-74	14.4106	Test 1	X							
July 22, 2001	9:09	13:09	39	28.3100	-74	14.0700	Sta X	X							X
July 22, 2001	10:40	14:40	39	27.5631	-74	14.7642	Sta X	X							
July 23, 2001	9:05	13:05	39	27.5448	-74	14.7788	Sta X	X							X
July 23, 2001	10:30	14:30	39	27.6786	-74	13.4737	PM5-A	X	X						X
July 23, 2001	12:10	16:10	39	27.9133	-74	12.2067	PM5-B	X	X						X
July 23, 2001	13:30	17:30	39	28.1311	-74	10.9268	PM5-C	X	X						
July 23, 2001	14:15	18:15	39	28.2786	-74	9.6649	PM5-D	X							
July 23, 2001	14:55	18:55	39	28.3987	-74	8.4116	PM5-E	X							X
July 23, 2001	15:36	19:36	39	28.5110	-74	8.3836	PM5-F	X							
July 23, 2001	16:30	20:30	39	28.5110	-74	8.3836	PM5-G	X							X
July 23, 2001	17:20	21:20	39	27.3552	-74	8.1331	PM5-H	X							
July 25, 2001	9:41	13:41	39	25.2385	-74	18.0101	AM4-A	X	X	X	X	X	X	X	X
July 27, 2001	16:05	20:05	39	31.0825	-74	20.1173	FISH-A	X	X						
July 27, 2001	16:24	20:24	39	31.0825	-74	20.1173	FISH-B	X	X						X
July 27, 2001	16:30	20:30	39	31.0825	-74	20.1173	FISH-C	X							
July 29, 2001	16:30	20:30	39	31.0825	-74	20.1173	FISH			X	X	X	X	X	X
July 31, 2001	9:35	13:35	39	31.0762	-74	20.1035	FISH-A	X	X						
July 31, 2001	10:18	14:18	39	31.0762	-74	20.1035	FISH-B	X	X						X
July 31, 2001	12:06	16:06	39	27.3896	-74	11.8295	Trans-end	SSC	X						X
July 31, 2001	12:52	16:52	39	27.5122	-74	14.8672	Node A	SSC	X						X
July 31, 2001	16:25	20:25	39	31.7873	-74	12.2002	Outside Front	X	X						X
July 31, 2001	17:18	21:18	39	33.5338	-74	13.4192	Inside Front	SSC	X						X
August 1, 2001	10:30	14:30	39	30.8624	-74	14.7774	01-A	X							
August 1, 2001	11:00	15:00	39	30.8624	-74	14.7774	01-B	X	X						X
August 1, 2001	12:19	16:19	39	31.6265	-74	10.9140	02-A	X	X						X
August 1, 2001	13:23	17:23	39	35.0887	-74	11.9799	03-A	X	X						X
August 1, 2001	16:15	20:15	39	27.5607	-74	14.8117	04-A	X	X						X
August 1, 2001	16:35	20:35	39	27.5607	-74	14.8117	04-B	X	SSC?						X
August 2, 2001	9:30	13:30	39	27.4334	-74	14.5871	01-A	X	X						X
August 2, 2001	11:17	15:17	39	23.9855	-74	15.9401	02-A	X	X						X
August 2, 2001	13:55	17:55	39	26.1816	-74	18.4562	03-A	X	X						X

Note: Optics profile consists of CTD, 2 ac9's, and HISSTAR

### 3. PREFLIGHT WAVELENGTH CALIBRATION

A laboratory wavelength calibration of the PHILLS-1 sensor was performed on July 11, 2001 by imaging oxygen, mercury, argon, and helium gas emission lamps. Each lamp produces emission lines at well-defined wavelengths, with the ensemble lines effectively covering the 400 to 1000 nm range. Data cubes were acquired at 512 spectral bands by observing each gas lamp for several seconds, and frame averaging the data to give sample-dependent spectra. Visual inspection of the line peak position for select lines as a function of sample number indicated that wavelength calibration was constant across the array within 1 to 2 nm. Consequently the data were summed over the central 800 samples or so of the array and the resultant spectral line profiles were fit (within ~25 spectral bands of the spectral line peak) with a Gaussian function and a quadratic background term. The exact in-air wavelengths of known emission lines were obtained using the atom.exe program from NIST. By pairing peak Gaussian band positions with known lines (see Table 3) a linear relation between 512-band number and wavelength was derived. This relationship is shown in Fig. 2(a). The corresponding bin-by-4 (or 8) wavelength is obtained from this linear relationship. The Full-Width Half Maximum (FWHM) of the Gaussian line width is plotted as a function of band number (wavelength) in Fig. 2(b). The detector FWHM decreases from ~ 2.7 nm at 400 nm to ~ 1.7 nm at 1000 nm wavelengths.

### 4. PREFLIGHT RADIOMETRIC CALIBRATION

A preflight radiometric calibration was performed on July 12, 2001. The basic process for performing a radiometric calibration is to have the sensor look at light sources spanning a range of known radiance and compare the observed signals in each spectral band of each cross-track spatial sample with the corresponding band radiance. The relationship should be linear, but small deviations are possible. Ideally, the radiance range of the sources should span what is observed in the field, but this is not possible at all wavelengths

Table 3 — July 11, 2001 Wavelength Calibration

Element	Wavelength	Band Center	FWHM (bands)
He	0.388865	6.885	2.630
Hg	0.404656	19.995	2.839
Hg	0.435833	45.612	2.689
He	0.447148	54.931	2.658
H2	0.486133	87.028	2.691
He	0.501568	99.727	2.616
Hg	0.546074	136.306	2.665
He	0.587568	170.504	2.455
H2	0.656272	227.011	2.386
He	0.667815	236.473	2.349
Ar	0.696543	260.016	2.271
He	0.706526	268.255	2.244
Ar	0.706722	268.401	2.251
He	0.728135	285.991	2.134
O2	0.777375	326.371	2.079
O2	0.844646	381.722	1.690
Kr	0.877675	408.905	1.686
Kr	0.892869	421.408	1.803
Ar	0.912297	437.368	1.827
Ar	0.922450	445.732	1.656
Ar	0.965778	481.361	1.894

Wavelength in microns  
Bands numbered 1-512

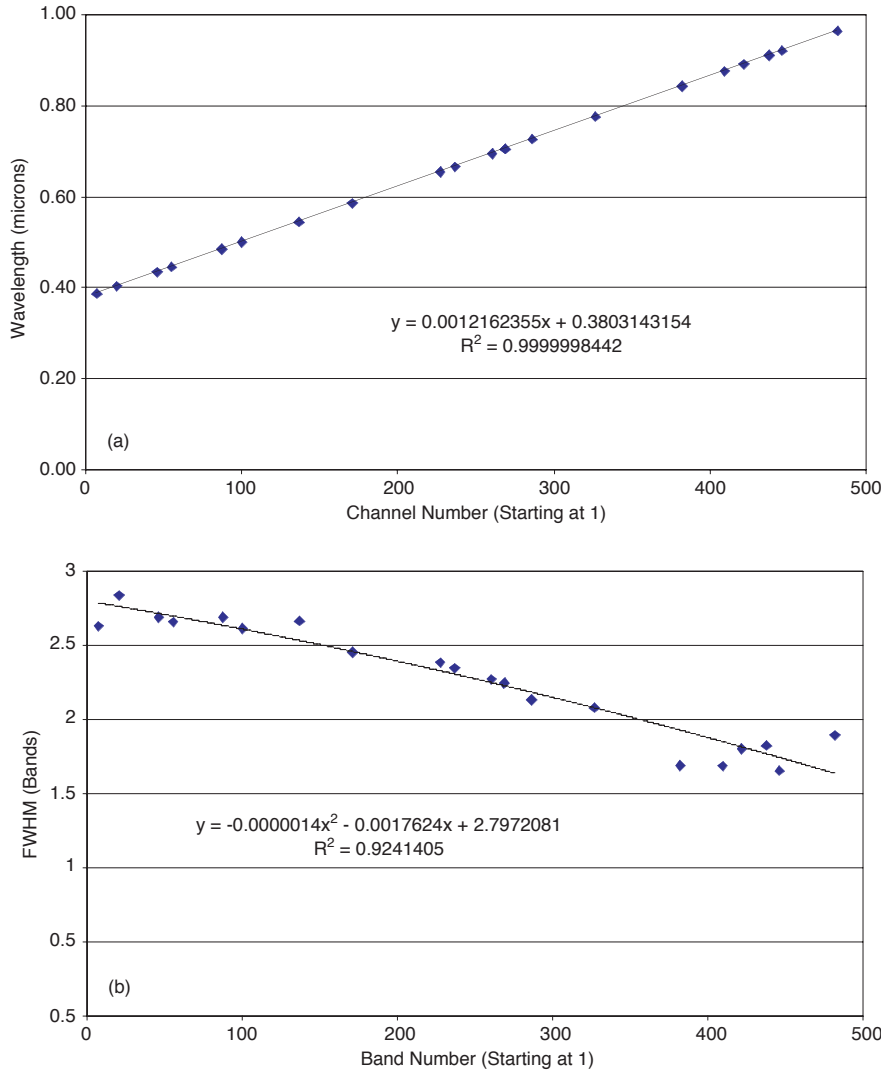


Fig. 2 — (a) Linear relationship between sensor channel (band) number and corresponding wavelength value. (b) Gaussian FWHM for wavelength fits showing change in Gaussian width vs band number.

because of the variety of targets that are observed (e.g., very dark blue-rich water and very bright red-rich sand). The laboratory light sources have a spectrum similar to a black body with a peak at 950 nm, and it is impossible to get large signals in the blue spectral channels without saturating the CCD in the red channels. Due to blooming and possibly scattered light effects, saturation of any part of the CCD affects the linearity of the pixels over the entire CCD. In these cases, it is necessary to extrapolate the radiometric calibration to signal levels outside of the range of the light sources.

One source used to calibrate the sensor is an integrating sphere containing a set of 10 quartz halogen lamps. The radiance is varied by powering different numbers of lamps. This method has been used extensively in the past [4], but the need to place a “blue-balancing” filter between the lamps and the sensor to prevent sensor saturation complicates the process.

For the LEO-15 2001 deployment, a different approach was used to calibrate the sensor. In this case, a range of radiance levels was obtained by varying the distance of a single light source from a diffuse plaque. The calibration setup is shown schematically in Fig. 3, where various geometric variables are shown. A

single NIST-calibrated FEL lamp (#fel399) was placed (a distance  $D$ ) from 40 cm to 120 cm from a well-characterized, spatially uniform, 99% reflectance Spectralon plaque (LABSPHERE SRT-99-100 #2). The plaque surface was oriented normal to the FEL-Plaque optic axis. This plaque was observed by the PHILLS-1 sensor from a 17 cm distance  $d$  at a 45 deg angle from the FEL-Plaque optic axis. The FEL lamp and PHILLS-1 sensor were carefully positioned so that the plane defined by the FEL lamp - Plaque - PHILLS-1 sensor optic axis was parallel to the optical bench. The sensor slit was oriented normal to this plane. Each sensor pixel (sample) views the plaque at a different distance  $h$  above (or below) the optic axis. This distance  $h$  was determined by knowing the distance of the plaque from the sensor  $d$  and the view angle  $\theta$  for each pixel. The view angle  $\theta$  was determined for each pixel by imaging a carefully measured grid pattern from a known distance. The radiance at any angle  $\theta$  is then given by

$$\text{Radiance}(\theta) = (\text{Irr50}/\pi) * (50\text{cm}/D')^2 * r_{\text{plaque}} \quad (1)$$

where  $D'^2 = (d * \tan(\theta))^2 + D^2$ ,  $r_{\text{plaque}}$  is the reflectance of the plaque at 45 deg interpolated to PHILLS-1 wavelengths, the plaque is assumed to be Lambertian, and Irr50 is the NIST-measured irradiance of the FEL lamp at 50 cm. Both the lamp irradiance and plaque reflectance depend upon wavelength.

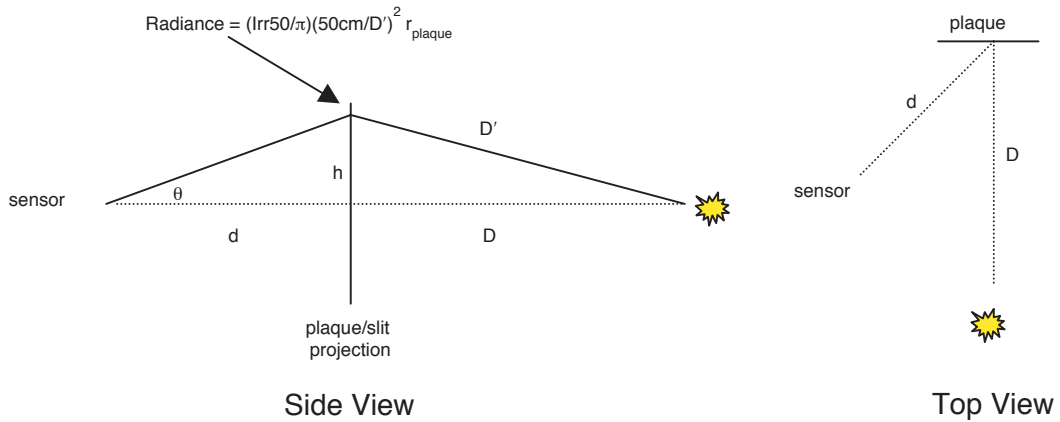


Fig. 3 — A schematic showing the physical layout for the PHILLS-1 radiance calibration. Irr50 is the NIST measured lamp irradiance at 50 cm from the light source,  $D$  is the distance of the light source from the plaque,  $d$  is the sensor distance from the plaque, and theta ( $\theta$ ) is the view angle of the plaque for each sensor pixel. The sensor slit is oriented perpendicular to the light source – plaque – sensor plane.

Potential complications are that the reflectance plaque is not truly Lambertian and the FEL light source, while small, is not truly a point source. On the optic axis, the FEL acts as a point source, and for the 45 deg viewing geometry, the slight non-Lambertian property of the plaque is known. However, for off-axis points, variations from the on-axis values become progressively greater. Unfortunately, no complete set of measurements exists to determine both effects at all lamp distances. However, another set of laboratory measurements can be used to partially compensate for these effects.

A series of measurements [10] was collected with a custom-built SPX425 spectrometer (this instrument has a 400 to 900 nm bandpass with 500 0.1 nm bands) along the centerline of the Spectralon plaque with the FEL lamp positioned at 50 cm as used in the PHILLS-1 radiance calibration. The SPX425 was mounted at 45 deg to the plaque on an optical bench quality “scissor jack” in roughly the same configuration as PHILLS-1. The SPX425 has a small 2.5 deg FOV, and was positioned about 10 cm from the plaque, so that the spectrometer viewed a relatively small area of the plaque ( $\sim 40$  PHILLS-1 spatial pixels) at any single jack position. The spectrometer was visually aligned to the center of the target and roughly optimized to the maximum signal. Spectra were then collected at nine vertical jack positions. The sampling sequence was the

center position (26.2 cm) +1.6, +3.1, +4.5, -3.5, -5.2, -7.3, -9.2, and -10.8 cm. The spectra were then normalized to the center measurement. It was found that this ratio for any given measurement was independent of wavelength at the 1% level. The observed ratio was then divided by the ratio expected purely on geometric grounds. The resultant correction factor as a function of angle off the optic axis is shown in Fig. 4. These points were then fit to a quadratic function of angle. The radiance calculated using Eq. (1) was multiplied by this function. This measurement geometry does not exactly match the PHILLS-1 sensor calibration geometry, but it is important to note that the lamp-plaque-sensor angle (which defines the plaque BRDF angle) is always close to 45 deg and differs by less than 0.1 deg between the two measurements at the furthest point off the optic axis (and vanishes to zero on the optic axis). Thus, plaque BRDF changes are likely to be minimal and the variations that are measured are likely caused by the non-point nature of the light source. This correction, although applied to all calibration measurements, is likely to be less important at larger lamp distances (lower counts). This may explain the small negative radiance offsets discussed in the next paragraph. Calibration of field data validates this correction factor, as cross-track radiances at long wavelengths (where atmospheric contamination of the radiance signal is smallest) are flat over uniform water scenes.

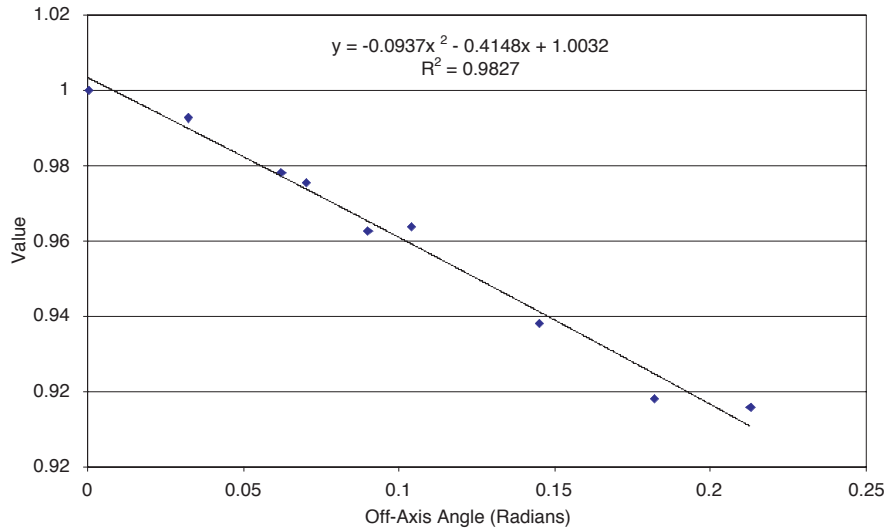


Fig. 4 — The plaque/lamp correction factor measurements and the quadratic fit to the data

Radiance calibration measurements were made with the FEL lamp distance to the plaque ranging from 40 to 120 cm, at 10 cm increments. The 50 cm position is set using a standard 50.000 cm rod. The FEL lamp is mounted on a 1-m AEROTECH stage. The other positions are achieved by moving the stage, which has a claimed accuracy of 1  $\mu$ m. Measurements were made with the camera lens, frame rates, and spectral binning as planned for the field experiment. The observed dark subtracted counts (corrected for frame transfer, see Section 5) for each spectral band of each spatial sample were then compared to the predicted radiances and a quadratic curve fitted to this data (see Fig. 5). The radiance fit was forced to go through zero at zero counts, although small offsets at the  $-0.05$  to  $-1.5$   $\text{W m}^{-2} \text{ sr}^{-1} \mu\text{m}^{-1}$  level are formally allowed. The best-fit coefficients were then stored in a 1024 sample  $\times$  (128 or 64 line)  $\times$  3 band (one band for each quadratic coefficient) Band Sequential (BSQ) calibration file for each sensor setting. Two calibration coefficient files exist for the bin-by-4 (25 fps) data, one for the original 128 channel data, and one for the summed 64 band data. This latter calibration file was computed by first summing adjacent bands in the original 128-band count data to 64 bands before applying a quadratic fit to the predicted radiance.

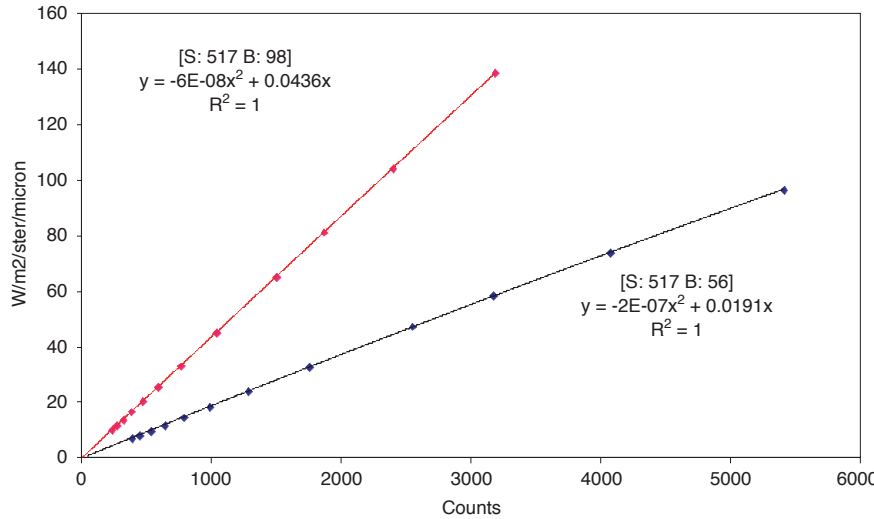


Fig. 5 — Example of quadratic equation fits to radiance calibration data for July 12, 2001. The best-fit quadratic equation coefficients are forced to pass through zero. Although a quadratic equation is used to fit the data, the quadratic term is much smaller than the linear part of the function.

## 5. CORRECTION OF SENSOR COUNTS FOR FRAME TRANSFER

The PHILLS-1 sensor counts have to be corrected for frame transfer before data can be calibrated or calibration coefficients determined. The reason is that the sensor never really stops collecting photons and continues collecting even while data are being transferred (read) out of the CCD array. Data are read out of the array sequentially in wavelength (or band) space. One can think of the CCD bands as “buckets” on a conveyor belt that are moved into the active CCD area, stay stationary for some time, and then are transferred out of the active CCD area. The time for this to occur is  $T = 1/f$ , where  $f$  is the camera frame rate. The effect of frame transfer is to distribute a small fraction of the true counts (TRUE) of each spectral band into all the other bands. Thus, in order to determine correct calibration coefficients that relate true counts in a band to radiance in that band, the true count must be determined for each band by “putting back” misplaced counts that were put into the wrong bands and removing counts that really belong in other bands. This correction can be **precisely** accomplished because even though counts are redistributed spectrally, the total spectral count (TOTAL) is conserved.

The effects of frame transfer are most clearly demonstrated if one does a “thought experiment” where the true spectrum is a delta function in wavelength space. If one frame of data is taken, and frame transfer did not occur, one would observe all the counts (TOTAL  $\equiv$  TRUE) in a single band and all the other bands would be identically zero. TRUE is collected in time  $T = 1/f$ . If, however, part of this time  $\tau$ , where  $\tau$  is the frame transfer time, is spent transferring the bands (N) into and then out of the active CCD detector area, then the count observed in each of the other bands would be  $C = (\text{count rate}) \times (\text{time spent in a wrong band}) = (\text{TRUE}/T) * (\tau/(N-1)) = (\text{TRUE}/(N-1)) * f * \tau$ . The probability that a count ends up in a single wrong band is

$$\text{PROB} = C/\text{TRUE} = f * \tau / (N-1). \quad (2)$$

For PHILLS-1, the frame transfer time is on the order of 1.5 ms. Therefore, the probability of misplacing a count in 64-band data with a camera frame rate of 25 fps is 0.0006, and is 0.0011 for a 46 fps camera rate. While these probabilities are small, they are not insignificant and can have a profound effect, especially in bands with few intrinsic counts.

This type of analysis can be generalized to any spectrum. In this case the observed count (OBS) in any band is given by

$$\text{OBS} = \text{TRUE} - \text{OUT} + \text{IN}, \quad (3)$$

where TRUE is the true count that belongs in the band, OUT is the count that is incorrectly placed into other bands, and IN is the count from other bands that is incorrectly placed into the band in question. Now  $\text{OUT} = \text{TRUE} \cdot \text{PROB} \cdot (N-1)$ , where PROB is given by Eq. (2). Because total count (TOTAL) is conserved,  $\text{IN} = \text{PROB} \cdot (\text{TOTAL} - \text{TRUE})$ . Substituting these into Eq. (3) and rearranging terms gives

$$\text{TRUE} = (\text{OBS} - \text{PROB} \cdot \text{TOTAL}) / (1 - \text{PROB} \cdot N). \quad (4)$$

Thus, the true count can be precisely recovered for any band if one knows the value of PROB.

While one can obtain an estimate of PROB using general sensor characteristics (e.g., the estimates given earlier), it is more accurate to obtain this value directly from the sensor data itself. One way this has been done is to observe a laboratory calibration lamp with and without a red-filter placed over the sensor lens, and then dividing the red-filtered data by the unfiltered data. This ratio should replicate the red-filter transmission function. Frame transfer effects would cause deviations from that shape. Shown in Fig. 6 is such an observation where the camera frame rate is set at 46 fps. The black curve is the ratio of the original data before correcting for frame transfer. The red curve is the expected red-filter transmission function. The observed ratio clearly exhibits deviations from expected at both blue and red wavelengths. The blue curve shows the ratio of the same data set, but where the observed counts have first been corrected for frame transfer using a PROB value of  $13.2 \times 10^{-4}$ . This value is in good agreement with the estimate made earlier. A PROB value of  $7.7 \times 10^{-4}$  provides good agreement with 64 band 25 fps data.

All LEO-15 2001 laboratory and field data are corrected for frame transfer using these probability values. Examples of calibrated field data both as collected and corrected for frame transfer are shown in Fig. 7(a), and the effect this has on atmospherically corrected derived  $R_{rs}$  is shown in Fig. 7(b).

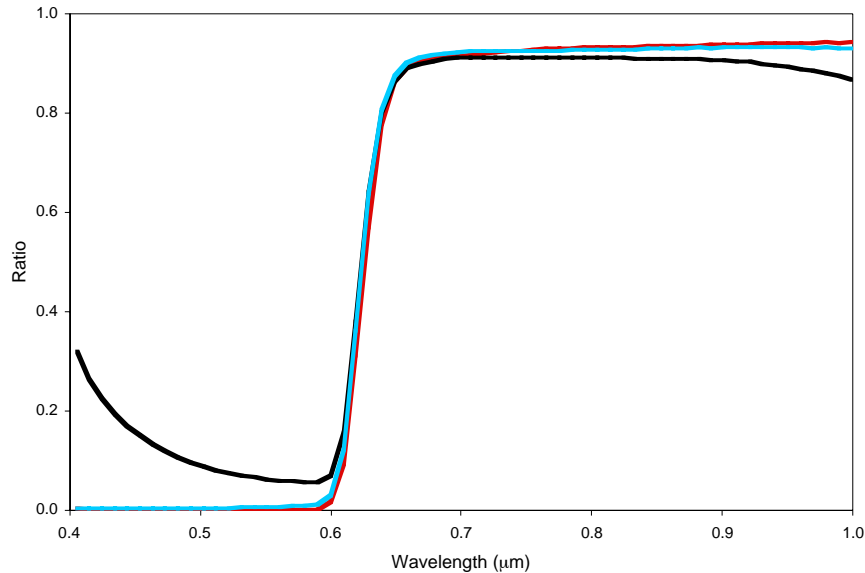


Fig. 6 — The ratio of the red-filtered divided by unfiltered calibration data for one of the central pixels in the sensor array. The black curve is the original measurement not corrected for frame transfer. The blue curve shows the same data, but correcting for frame transfer assuming  $\text{PROB} = 13.2 \times 10^{-4}$ . The red curve is the expected red-filter transmission function.

## 6. ADJUSTMENT OF LABORATORY CALIBRATIONS TO MATCH FIELD DATA

Data collected in the field are grouped into  $1024 \text{ sample} \times 1024 \text{ line} \times (128 \text{ or } 64) \text{ band}$  BIL format files. The sensor has an intrinsic 12-bit dynamic range and data are bit-shifted and stored in the BIL file as a 16 bit (2 byte) scaled (by 4) integer. This data grouping is called a sequence, with a time contiguous group of sequences composing a data run. A dark file is taken at the end of each run.

The process of calibrating the field collected count data into physical unit radiance values begins with averaging the dark file for the run in the line (time) dimension to obtain an average dark current spectrum for each sensor sample. This time-averaged spectrum is then subtracted from each line in the data file. We have

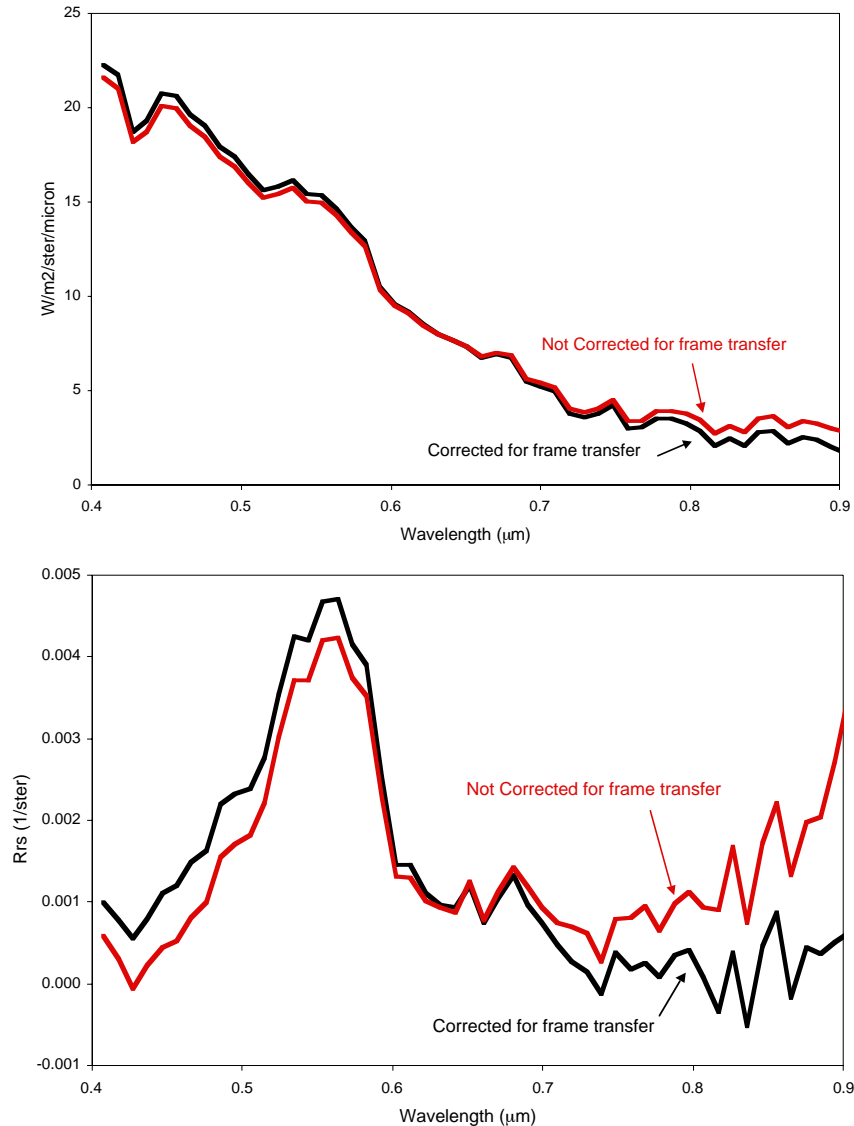


Fig. 7 — (a) The calibrated spectrum of a deep-water pixel observed off the coast of New Jersey at LEO-15. The red curve is the data without correcting for frame transfer and the black curve is the spectrum for the same pixel but correcting for frame transfer. Note the differences in radiance at both long and short wavelengths. (b) Atmospherically derived remote sensing reflectance ( $R_{rs}$ ) for same pixel. The black/red curve has not been corrected for frame transfer. The uncorrected spectrum exhibits lower reflectance at short wavelengths and a rising reflectance at long wavelengths.

found that for PHILLS-1 the sensor dark current typically changes less than 2 counts during the data run. This change typically corresponds to a radiance of  $0.02$  to  $0.15 \text{ W m}^{-2} \text{ sr}^{-1} \mu\text{m}^{-1}$ , depending upon wavelength over much of the detector, and corresponds to about 5% of the radiance observed at wavelengths greater than 700 nm (and is much smaller at shorter wavelengths). Each frame transfer corrected dark subtracted spectrum (count) for each spatial pixel must then be multiplied by the applicable calibration coefficient BSQ file to be converted into radiance units. The radiance file is typically stored as a 16-bit (2 byte) 1000 sample  $\times$  1024 line  $\times$  64 band scaled (by 100) integer BIL file. One thousand samples, rather than the 1024 available, are typically calibrated because of dead-pixels and uncertain calibration at each end of the detector array.

Ideally, laboratory calibrations will match the field data identically, and the laboratory calibration coefficient files are directly used to calibrate the field data. Occasionally there are small spatial and spectral shifts between field- and laboratory-collected data and these differences must be accounted for in order to use laboratory calibrations to properly calibrate data collected in the field. The reason for these shifts is unknown, but they can be corrected by transforming laboratory wavelength and radiance calibration results to match field conditions.

A spatial shift of about 1 pixel (one sample) was required to match laboratory and LEO-15 2001 field conditions. This is shown in Fig. 8, where the top plot is from the laboratory radiance calibration made on July 12, 2001. The dark vertical lines result from imperfections in the spectrometer slit. The amount of light recorded is related to the width of the slit and more or less light is seen because of bumps and indentations in the slit width. The image below is taken from data collected in the field. The same vertical banding is evident in this image, but close inspection shows that the slit patterns are offset from each other. The top image (that is, the calibration coefficients) must be shifted 1 pixel to the right to match the in-field slit pattern.

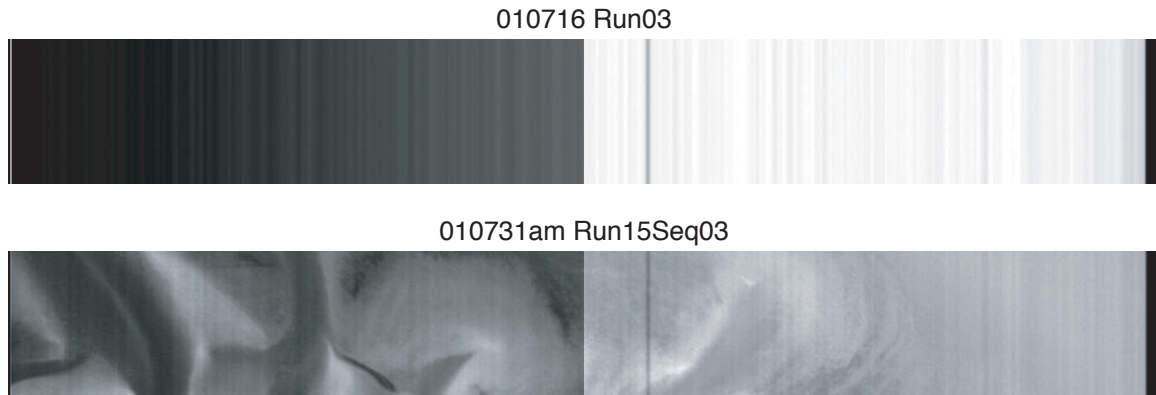


Fig. 8 — The top image is raw data from a laboratory calibration that was taken on July 16 prior to the LEO-15 2001 deployment. The “banding” structure is caused by imperfections in the spectrometer slit. The bottom image is the first 128 lines of the observed counts collected during the field deployment on July 31. A careful comparison of the slit “banding” structure indicates that there is a 1-pixel spatial shift during the deployment.

A spectral shift of about 2.6 nm is also required to match laboratory and field conditions. This is shown in Fig. 9, where a spectrum of the sky taken with an Analytical Spectral Devices (ASD) spectrometer is compared with the radiance spectrum observed over land by PHILLS-1, where the laboratory wavelength calibration has been assigned to the PHILLS-1 data. Note that the position of the oxygen absorption line at  $0.76 \mu\text{m}$  is different in the two spectra. There are other features in these spectra that can be compared, including the solar absorption feature at  $0.43 \mu\text{m}$  and the atmospheric water vapor absorption feature at  $0.82 \mu\text{m}$ . The ASD spectrum shows these features at their true wavelengths. The differences between observed and assigned band positions for these and other spectral features can be fit with a linear function to transform laboratory band wavelength assignments to in-the-field band positions.

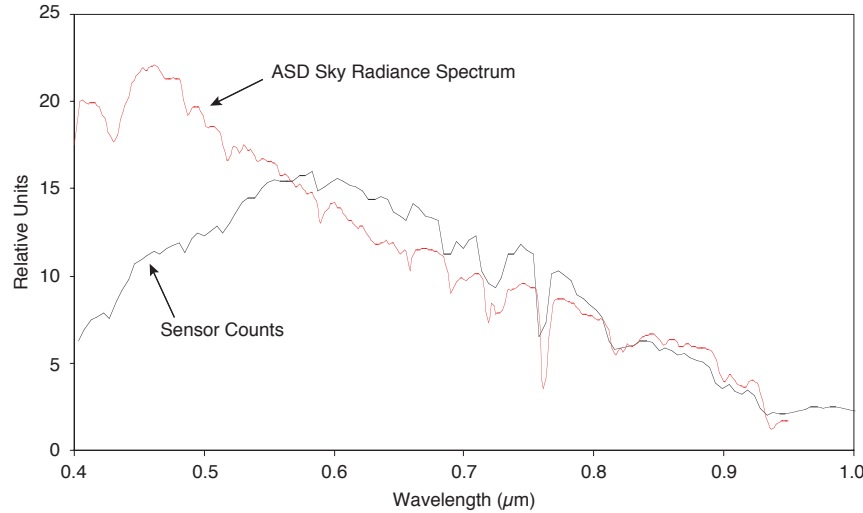


Fig. 9 — The black curve is a spectrum of an observed land pixel from the PHILLS-1 sensor at LEO-15. The wavelength assignment is from the laboratory wavelength calibration that occurred prior to deployment. The red curve is an ASD spectrum of the sky obtained from the ground. Note the difference in position of the  $O_2$  absorption feature at  $0.76 \mu\text{m}$ . The in-field sensor wavelengths have shifted compared to the laboratory values.

Both spatial and wavelength transformations are applied to the radiometric calibration coefficient files. The spatial correction is a single sample offset adjustment. The wavelength calibration adjustment is a simple linear band transformation. The calibration coefficient files are first shifted spatially and then spectrally. This requires resampling the laboratory calibration coefficient matrix to the equivalent in-the-field position in both the sample and band dimensions. It is the resampled laboratory radiometric calibration coefficient file that is applied to the field count data to assign radiance units to each field-acquired spatial pixel spectrum.

## 7. SCATTERED LIGHT NEAR BRIGHT LAND FEATURES

There is one detector systematic effect we have not yet corrected for. This is scattered light, probably occurring within the sensor, which becomes apparent when a dark water pixel is located near bright land. This is shown in Fig. 10, where we show a single band ( $0.99 \mu\text{m}$ ) data sequence collected on July 31, 2001, as we passed over Seven Islands in Great Bay, New Jersey. An equalization stretch has been applied to the image in order to make apparent this effect. The bright land features are clearly delineated. Water pixels are dark in this image because there is little water leaving radiance at this wavelength. Note, however, that there is a brightening for those water pixels located close ( $\sim 50$  to  $100$  pixels) to land. While atmospheric scattering could cause such an effect [11], the scattered light appears to be oriented parallel to the sensor slit, suggesting that light scattering is occurring within the sensor. The amount of scattered light is small ( $\sim 10^{-4}$  peak signal), but is great enough to effect the near-IR remote sensing reflectance for these pixels. This effect is small below  $0.7 \mu\text{m}$ , but caution should be exercised when analyzing the near-land, near-IR wavelength spectra.

## 8. DATA GEOREFERENCING

The aircraft's Global Positioning System (GPS) latitude, longitude, altitude, pitch, roll, heading, and time were determined at a rate of 10 entries per second using the inertial navigation system in a C-Migits II GPS/INS device (BEI Technologies Systron Donner Inertial Division, Concord, California). Sensor soft-

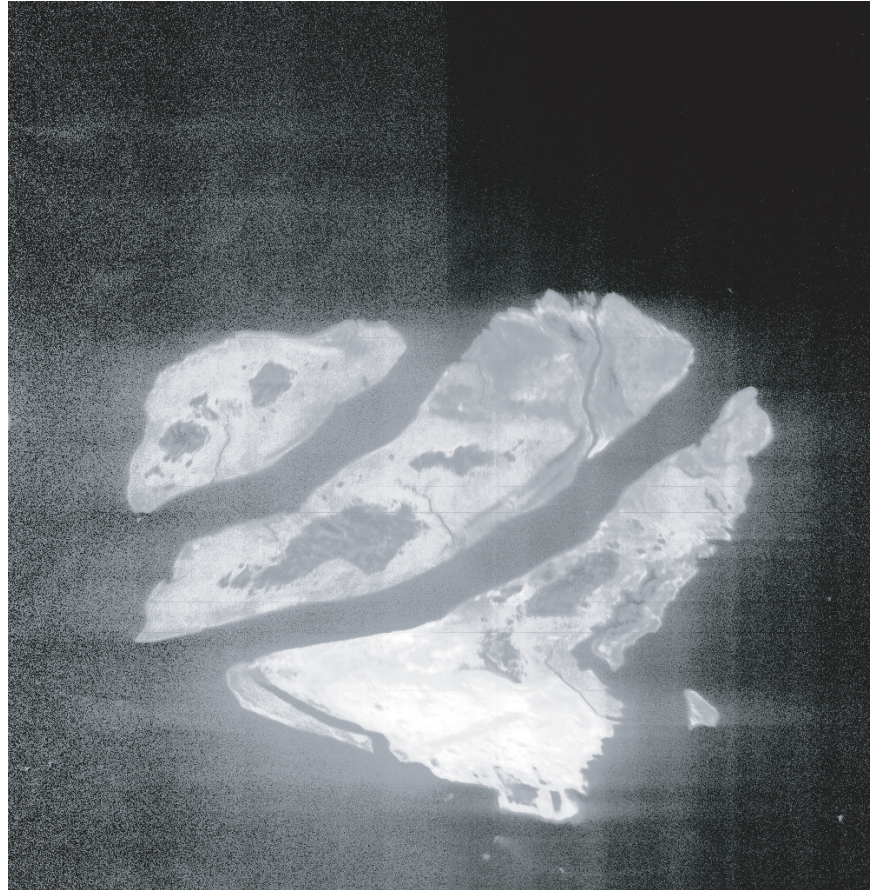


Fig. 10 — Equalization stretch of  $0.99 \mu\text{m}$  image showing scattered light near bright land features. The scattered light appears to be oriented in the horizontal direction, parallel to the sensor slit, suggesting that scattering is occurring within the sensor. The amount of scattered light is small ( $\sim 10^{-4}$ ), but is great enough to effect the near-IR remote sensing reflectance over nearby water pixels, which should be extremely dark at these wavelengths.

ware is responsible for writing sensor data to a mass storage device and time-tags each frame (line) of data with the GPS time at that instant. Twenty-five (or 46) frames of sensor data were written per second, depending on camera frame rate. By noting the time a frame was written, it is possible to interpolate C-Migits data information to depict the plane (that is, the C-Migits device) position, altitude, and orientation at that time. If one also knows the angular offset of the sensor optic axis relative to the C-Migits device and the angular offset (view angle) of incoming light for each sensor pixel (sample) from the optic axis, it is then possible to calculate the longitude and latitude of each sensor pixel at the time the data were taken.

Once the sensor is placed (bolted) into the plane, the sensor orientation offset should be the same for each data run. Given the accuracy of input information and our interpolation procedure, it should be possible to determine the ground coordinates of each pixel in the PHILLS-1 image to an absolute accuracy of about 5 pixels.

A mapping of the angle of incoming light for each sample on the detector array, called a pointing or view geometry file, was determined as part of the laboratory calibration. Using a set of Ground Control Points (GCPs) at LEO-15, we determined the fixed roll, pitch, and yaw (heading) orientation offset of the sensor from the C-Migits device by comparing the known GCP positions with those observed. A nonlinear least-square algorithm was used to find the offsets that minimized the RMS positional error for these points. The

GCPs were identified from a 1-m ground truth image of the area constructed from digital aircraft photographs provided by Richard Lathrop [12] and supplemented with digital images downloaded from the TERRASERVER [13] website.

The sensor physical orientation roll, pitch, and heading offsets for LEO-15 are listed in Table 4. Because an error in pitch can manifest itself as an apparent error in time, we can improve the positional accuracy for each pixel location by determining a “time offset” for each data run. In determining the time offsets, the GCPs are derived from as large an area as possible. If the resultant RMS error between known and best-fit positions is less than 5 pixels, then a single time offset is adequate for that run. In some cases, however, the data could not be adequately fit over the length of a data run with a single time offset. In these cases, the data run was divided into smaller sequential pieces to compute time offsets for those sequences. It appears that this is necessary mainly for the high frame-rate (46 fps) data runs. A possible hint as to why different time offsets are necessary during a data run is shown in Fig. 11, where discontinuities in the image are apparent. This type of discontinuity is possible if one or more data frames are not recorded (that is missing or dropped) for some reason. At present it is not clear how this occurs. Other data discontinuities have been noted, and it is possible that others may not be apparent (such as over water or some amorphous land area). Thus, the claim of 5-pixel accuracy over water-only regions should be treated with some caution. Table 5 lists the time offsets for various data runs.

The C-Migits data and the physical and time offsets are used to generate an Input Geometry (IGM) file that provides the latitude and longitude of each pixel in an image. An IGM file can be produced for each sequence in a data run for which C-Migits data are available. This information can then be used to georectify an image to remove distortion caused by aircraft motion. ENVI [7] uses the IGM file, for example, to produce a Graphics Lookup Table (GLT) file that provides the information necessary to quickly warp the image (or any product derived from it) to a geographic coordinate system. An example of a georectified PHILLS-1 image is shown in Fig. 12. The nonrectangular shape of the border of the georectified image shows the amount of warping that was applied to remove aircraft motion from the image.

Table 4 — Sensor Orientation Offsets  
for Image Geo-Referencing

Roll	0.401 deg
Pitch	-0.3451 deg
Heading	0.676 deg
Altitude	-35.51 m
Magnification	0.971

Table 5 — Sensor Time Offsets for Image Geo-Referencing

Day	Run	Sequence	GCP RMS Error (m)	Time Offset (s)	Comments
23 July 2001	01	00-06 07-12	4.321	0.967	no GPS
	04		9.946	1.031	
	06		5.495	1.325	no GPS
	08		5.111	1.039	
	11		7.284	1.300	
	13		9.841	1.145	
	16		9.812	1.201	
	20				no GPS
	22				

Table 5 (continued) — Sensor Time Offsets for Image Geo-Referencing

Day	Run	Sequence	GCP RMS Error (m)	Time Offset (s)	Comments
25 July 2001	00		4.552	0.978	Turbulence Problem
	02		4.824	1.360	
	04		5.919	1.095	
	06		13.760	1.348	
	08				
	10		5.306	1.256	
	12		5.313	1.186	
27 July 2001	00	02-04	4.532	2.296	
		13-14	4.997	2.815	
	02		4.982	2.891	
	04	01-06	4.0025	2.852	
		07-08	3.963	3.629	
		08-11	4.446	3.974	
		14-15	4.575	3.140	
	06		4.545	2.393	
	08		4.973	2.269	
	10		4.621	2.150	
	12		4.016	2.409	
	14		4.696	2.194	
	16		4.083	2.417	
	18		4.441	2.247	
	20		3.288	2.539	
31 July 2001	22		4.940	2.349	Interpolated
	25		5.065	2.347	
	27		4.456	2.316	
	29		4.076	2.425	
	31		3.594	2.334	
	03		6.631	11.363	
	05		10.745	11.030	
1 August 2001	07		7.064	10.300	
	09		13.640	10.602	
	11		12.480	10.539	
	13			10.310	
	15		6.463	10.149	
	02		6.833	1.325	
	04		14.081	1.901	
2 August 2001	06		5.288	1.516	
	08		8.945	1.411	
	10		7.467	1.900	
	12		11.735	1.301	
	02		4.732	1.300	
	04		3.407	1.145	
	06		3.728	1.201	
	08		4.557		
	10		3.246	0.978	
	12		4.898	1.360	
	14		3.612	1.095	
	00-08		4.532	1.348	
	09-14		4.896		
	15-17		4.862	1.256	
	16		4.669	1.186	

Table 5 (continued) — Sensor Time Offsets for Image Geo-Referencing

Day	Run	Sequence	GCP RMS Error (m)	Time Offset (s)	Comments
2 August 2001	19	02-06	4.676	2.296	
		07-09	4.728	2.815	
		10-12	4.704	2.891	
		14-15	4.548	2.852	
		16-18	4.435	3.629	
	21	00-05	4.487	3.974	
		09-13	4.501	3.140	
		23	03-05	4.899	2.393
		09-10	3.294	2.269	
		12	4.640	2.150	
		12-13	4.563	2.409	
		14-15	4.954	2.194	
		16	4.913	2.417	
		17-18	4.934	2.247	
	25		3.382	2.539	
		00-03	4.702	2.349	
		29	3.294	2.347	
		31	4.461	2.316	



Fig. 11 — Portion of an image showing two discontinuities (the locations are highlighted by the red colored arrows) apparently caused by “dropped lines” (lost data). The dropped lines appear to occur mainly in the high frame-rate (46 fps) 1-m spatial resolution data.

It is our experience that georectified images may need to be adjusted or warped yet again if better pixel accuracy is desired. For example, the area shown in Fig. 12 was observed on two separate flights. When georectified images of the central portion of this area were compared, they were found to differ by some 20 m in the longitude and latitude directions. An image-to-image transformation was used to warp the images to a common reference. Of course, such a transformation is possible only if there are well-defined positional points in the image. Images of uniform scenes, such as optically deep water, cannot be so corrected.

## 9. CALIBRATED PRODUCTS

Calibrated data are typically stored as 16-bit (2 byte) 1000 sample  $\times$  1024 line  $\times$  64 band integer BIL files. The units for each spectral band are  $\text{W}/\text{m}^2/\text{ster}/\mu\text{m}$  multiplied by 100. Each BIL file has an associated ENVI-compatible ASCII header file that contains information regarding the BIL file format. The wave-

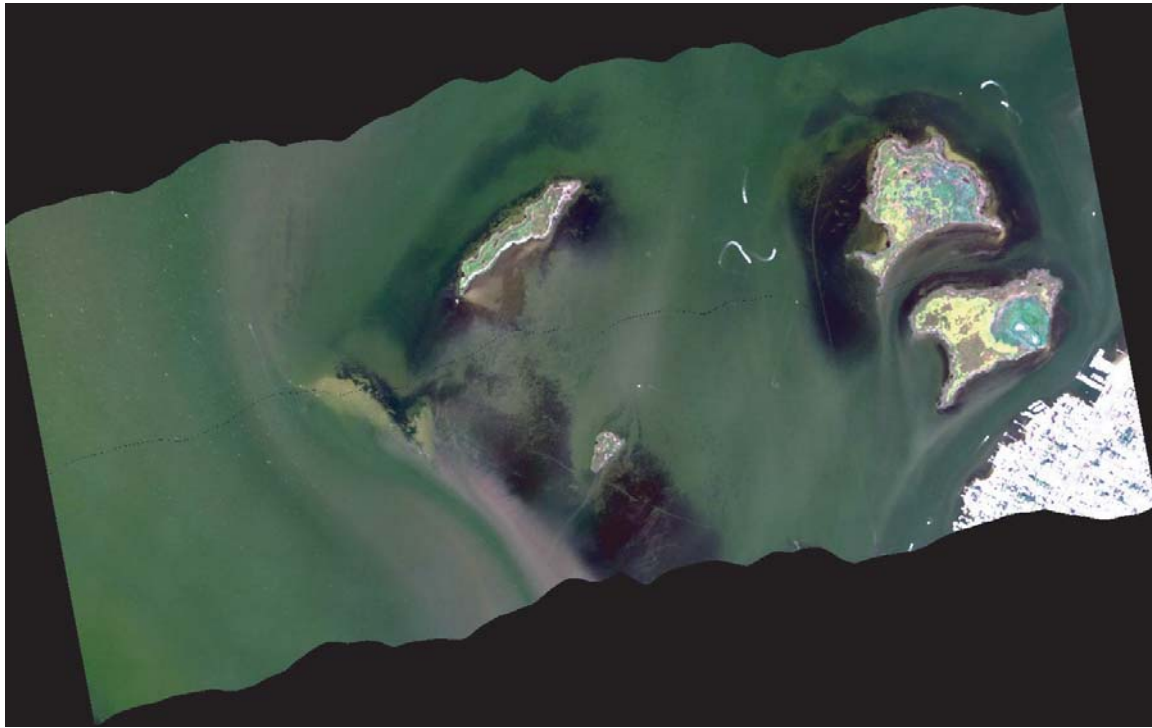


Fig. 12 — An example of a georectified image collected on July 23, 2001 over Barneget Bay, NJ. North is to the top and east is to the right. The area covered is approximately 2 km  $\times$  4 km.

length and FWHM for each spectral band are also included. Information regarding the observation date and *approximate* time, longitude, and latitude of the center of the image is also put into the header file. This information has nonstandard ENVI keywords associated with them and could be lost if an old version of ENVI is used to modify the header file. If C-Migits information is available for the data sequence, then an IGM file containing the same number of samples and lines as the calibrated file is also available.

Also available is a bad lines mask file. Occasionally data are found to be spectrally shifted one band to the blue or red wavelengths. This spectral shift is different than the general wavelength shift between laboratory and field data already discussed. When this occurs, it affects all samples within a single frame (line). The reason for this shift is unknown, but it is easily detected. Each data sequence is routinely processed to detect these bad lines (frames), and the output is a bad lines mask file. This file is a single-band BSQ file with the same number of samples and lines as the calibrated data file. The value for each pixel is zero (0), unless the frame (line) exhibits a spectral shift, in which case a value of 100 is assigned to each pixel in the line. There are typically only a few (< 10) bad lines per data sequence. Figure 13 is an example of a “Bad Lines” mask.

## 10. ATMOSPHERIC CORRECTION OF THE DATA

The standard product we produce is calibrated radiance; however, for many applications, the scientific analysis of the calibrated data requires atmospheric correction to give remote sensing reflectance. The atmosphere accounts for about 90% of the observed radiance for most aircraft and satellite optical remote sensing over water. Therefore, the accuracy of the result depends upon the accuracy of the model atmosphere used, the accuracy of the data calibration, and the identification and removal of sensor systematic errors. A discussion of atmospheric removal using an NRL-developed atmospheric algorithm, Tafkaa [14, 15], is presented here. This discussion is given in order to give the reader an appreciation of the issues involved in producing

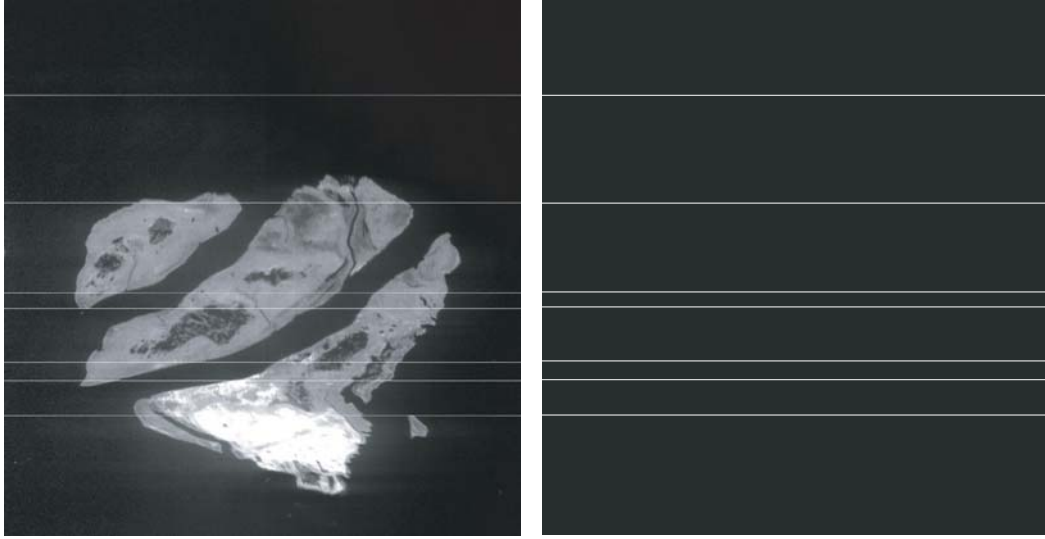


Fig. 13 — The image on the left is band 128 of Run 15 Seq 03 taken on July 31, 2001. The horizontal lines are caused by a 1-pixel spectral shift for spectra in those lines. The image on the right is the “bad-lines mask” created from it.

a remote sensing reflectance product, especially as they relate to PHILLS-1 data at LEO-15. Many issues, however, are applicable to all optical remote-sensing systems.

Unless all parameters of the atmosphere are known (and they rarely, if ever, are), atmospheric removal requires judgment on the part of the analyst. In Tafkaa, one must know the lighting geometry of the scene under consideration (that is, the solar orientation and the orientation of the sensor view direction relative to the Sun) to correctly account for the amount of sky light reflected directly off the water surface, and define the atmospheric parameters to be used including the aerosol optical properties of the scene.

Scene observation geometry is important because atmospheric absorption depends upon the path length the light must traverse first down to the surface and then back up to the sensor, and atmospheric scattering is a vector process dependent upon the scattering properties of the material and the direction of the incident light. The scene geometry can be accurately determined by knowing the location and time of the observation (which defines the solar zenith and azimuth angles), the altitude of the sensor, the direction (azimuth angle) the aircraft is traveling, and the view angle of the sensor relative to that of the aircraft. At LEO-15, the PHILLS-1 sensor points toward the Earth at nadir position. The field of view (FOV) of the sensor, however, is  $\pm 20$  deg and only the central pixel is pointed at nadir. Pixels at each end of the sensor array view  $\sim 6\%$  greater path length than those located in the center, and this causes a brightening in the blue part of the spectrum for those samples at each end of the array (see Fig. 14). Currently, Tafkaa assumes a constant geometry over the image, but a new version (still in testing) allows for changing view geometry. Flight lines are normally chosen to be flown into or out of the Sun to obtain uniform illumination across the scene. Misalignments in flight azimuth angle will sometimes occur and this can produce an asymmetric light variation across the scene. This is shown in Fig. 15(a), which shows sky reflection from the surface varying from left to right across the image.

In Tafkaa, the amount of reflected sky light is a function of the wind speed. Tafkaa uses the Cox-Monk formulation for a wind roughened sea surface as implemented by Ahmad and Fraser [16] to derive the amount of surface reflected light. Currently, wind speeds of 2, 6, and 10 m/s are supported. Note that sky reflection from surface capillary waves is modeled, but not the larger amplitude surface waves. At the high spatial resolution of the PHILLS-1 sensor, this larger spatial amplitude wave pattern can cause different



Fig. 14 — This RGB image was collected over deep water on July 23, 2001. The bluish color on each side of the image is caused by the wide angle field of view of the sensor, which sees a greater atmospheric path length on the sides of the image compared to that in the center.

amounts of direct and diffuse skylight to be reflected into the sensor from different portions of the wave. This is shown in Fig. 15(a), where the surface waves on the left side of the image are oriented at just the right angle to reflect more solar radiation into the PHILLS-1 sensor. Note also, that localized currents, bottom material, or local wind variations can disturb (or calm) the water surface and regions of localized enhanced (or depressed) surface reflectance are possible.

The 1976 U.S. Standard Model Atmospheres for tropical, sub-Arctic and high latitude summer and winter and the U.S. Standard 1962 atmosphere are currently supported in Tafkaa. Four basic types of aerosol model are also supported, consisting of varying proportions of large and small aerosol particles. An absorbing aerosol is also available [17]. The aerosol optical properties are defined by specifying the aerosol type, the relative humidity, and the aerosol optical depth (or visibility) at 550 nm. The choice of aerosol is especially important at short visible wavelengths, where aerosol scattering is especially dominant. If the aerosol properties of the scene are not known, then one must choose the aerosol model to use.

It is possible to use wavelengths greater than 700 nm to help determine the aerosol type by assuming that the water leaving radiance at these wavelengths is zero. Tafkaa can be run in such a mode, in which case one can choose a set of wavelengths where atmospheric absorption is known not to be important and Tafkaa then picks the aerosol model that best matches the observed signal. For PHILLS-1, which has an upper wavelength bound of 1000 nm, there are only two wavelength regions (0.750 and 0.865  $\mu\text{m}$ ) suitable for this

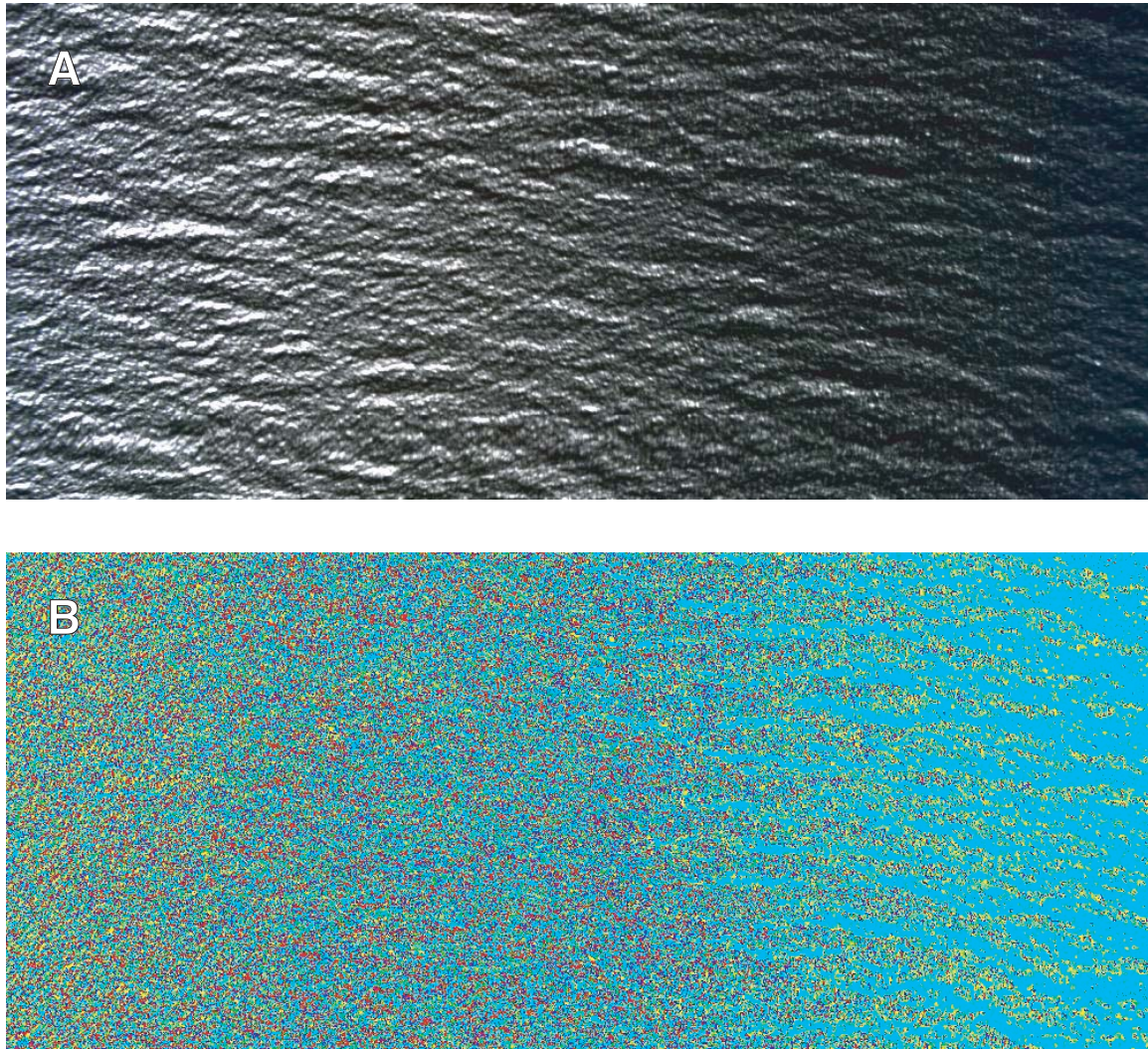


Fig. 15 — (a) This image was taken at the end of Run 15 on July 31, 2001. At the time of the observation, the Sun was high in the sky. An asymmetric surface glint pattern is evident and is caused by a slight misalignment of the aircraft flight line and solar azimuth angles. (b) The asymmetric light field and surface waves affect the best-fit aerosol model if Tafkaa is run on a pixel-by-pixel method. Here we have color-coded the best-fit aerosol model for each pixel. In this case, the change in surface glint amount is interpreted by Tafkaa as a change in aerosol model.

approach. With AVIRIS data, there are an additional four bands at longer wavelengths that could potentially be used. When Tafkaa is used in this mode, the output reflectance image is accompanied by a product file that lists the best fit aerosol model, optical depth, and humidity for each pixel.

Of course, this approach assumes that any observed signal in the bands chosen is caused by atmospheric scattering. Surface reflection effects can however be incorrectly interpreted as aerosol emission. This is shown in Fig. 15(b) where we have plotted the best-fit aerosol type for each pixel assuming that emission at 0.750 and 0.865  $\mu\text{m}$  is exclusively atmospheric. The best-fit aerosol model is clearly spatially correlated with the reflected surface light pattern. In images such as this, we have found that the wave troughs give the best estimate of aerosol parameters. An approach that we typically use is to first run Tafkaa on an image where it picks the best-fit aerosol values, and then rerun Tafkaa using an aerosol model defined by the mean or most likely aerosol model parameters for those pixels least corrupted by surface reflection effects. A deep-water scene is chosen to do this, because the assumption of zero water leaving radiance at long wave-

lengths is more likely to be true in offshore than nearshore areas, where suspended sediments are likely to be present. Those aerosol parameters can then be applied to each inshore image. This approach assumes that the aerosol type and optical depth are the same for near- and offshore regions.

Figure 16 shows an example of how the choice of an aerosol model affects the derived reflectance. This spectrum was taken from within Great Bay and is located in a channel just north of the Rutgers Marine Field Station. The black points are the PHILLS-1  $R_{rs}$  spectrum assuming a maritime aerosol with optical depth of 0.120 (a value measured from a nearby location with a SOLAR LIGHT Sun Photometer). The choice of maritime aerosol was used to produce a minimal signal at long near-IR wavelengths. This spectrum agrees well with a surface  $R_{rs}$  measurement (the red solid curve) made with a shipboard ASD spectrometer taken at almost the same time and place. The ASD spectrum has had surface glint removed by forcing the reflectance to be zero at 900 nm wavelengths. However, if these atmospheric parameters are applied to a deep-water scene located at the end of the run, it overcorrects for atmospheric effects and negative reflectances are derived. If this same offshore scene is used to derive the best-fit aerosol parameters, then an urban aerosol is preferred with optical depth of 0.093. If these parameters are then used to atmospherically correct the inshore data, then the green data point spectrum is derived. This spectrum is larger than that obtained with the ASD, but is more in line with the original ASD measurement before correcting for surface reflected light (the blue curve in the figure). In the relatively swift turbid water of Great Bay, it is not *a priori* clear that forcing the reflectance to zero at long wavelengths is the correct thing to do.

It is interesting to note, however, that the PHILLS-1 derived  $R_{rs}$  curves generally agree with each other if a constant offset is applied to one spectrum relative to the other in order to force agreement at long wavelengths. The spectra tend to track each other rather closely with differences being greatest at shorter wavelengths. We have found this to be true of other image spectra as well. This implies that errors in atmospheric and surface reflection correction tend to produce, to first order, systematic offsets. Relative changes in reflectance are probably not greatly affected, but parameters derived from them will mainly be changed in absolute scale.

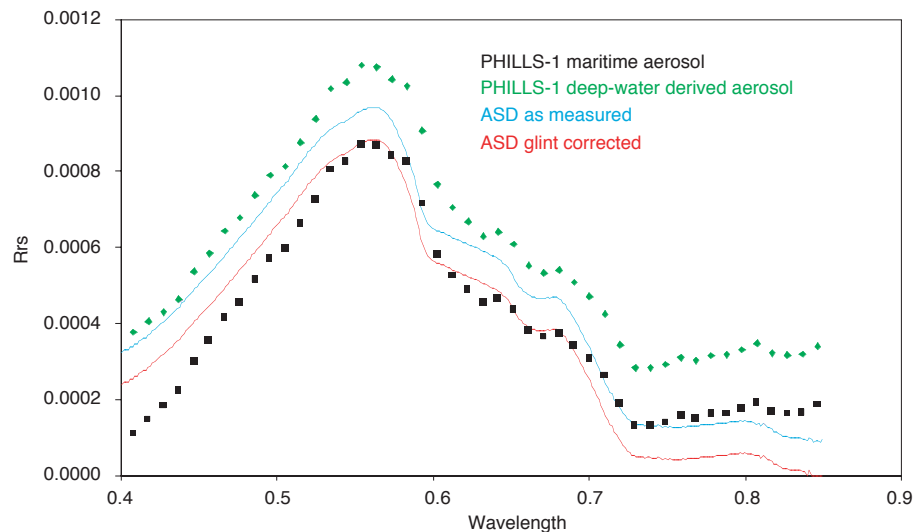


Fig. 16 — A comparison of PHILLS-1 derived remote sensing reflectance with near-simultaneous ASD reflectance measurements. The black points are the PHILLS-1 spectrum assuming a maritime aerosol. The green points are the PHILLS-1 spectrum using Tafkaa to derive aerosol parameters from an offshore deep-water scene. The blue and red lines are the ASD measure spectrum with and without glint removal.

## 11. ACKNOWLEDGMENTS

This research was supported by the U.S. Office of Naval Research. Our thanks in particular go to Joan Cleveland and Steve Ackelson for managing the HyCODE program. We thank Richard Lathrop of Rutgers University for providing the 1-m resolution ground truth image of the area, and Bob Steward and Dave Kohler of the Florida Environmental Institute for supplying calibration data for approximating the off-axis calibration correction. Jim Boschma and Mike Ryder skillfully piloted the AN-2 aircraft during the data collection.

## REFERENCES

1. Office of Naval Research (ONR) Hyperspectral Coupled Ocean Dynamics Experiment (HyCODE) program, <http://www.opl.ucsd.edu/hycode.html>.
2. The Long-term Ecosystem Observatory (LEO-15), <http://marine.rutgers.edu/cool/LEO/LEO15.html>.
3. D. Kohler, W.P. Bissett, C.O. Davis, J. Bowles, D. Dye, R.G. Steward, J. Britt, M. Montes, O. Schofield, and M. Moline, "High Resolution Hyperspectral Remote Sensing Over Oceanographic Scales at the LEO-15 Field Site," *Ocean Optics XVI* (Office of Naval Research CD), November 2002.
4. R.A. Leathers, T.V. Downes, W.A. Snyder, J.H. Bowles, C.O. Curtiss, M.E. Kappus, W. Chen, D. Korwan, M.J. Montes, W.J. Rhea, and M.A. Carney, "Ocean PHILLS Data Collection and Processing: May 2000 Deployment, Lee Stocking Island, Bahamas," NRL Formal Report NRL/FR/7212-02-10,010, May 2002.
5. C. Davis, M. Kappus, J. Bowles, J. Fisher, J. Antoniades, and M. Carney, "Calibration, Characterization and First Results with the Ocean PHILLS Hyperspectral Imager," *Proc. SPIE* **3753**, 160, 1999.
6. C. Davis, J. Bowles, R.A. Leathers, D.R. Korwan, V.T. Downes, W.A. Snyder, W.J. Rhea, W. Chen, J. Fisher, P.W. Bissett, and R.A. Reisse, "The Ocean PHILLS Hyperspectral Imager: Design, Characterization, and Calibration," *Optics Express* **10**(4), 210, 2002.
7. The Environment for Visualizing Images (ENVI), Research Systems, Inc., <http://www.ResearchSystems.com/envi>.
8. NRL Optical Sensing Section, IR/Radio/Optical Sensing Branch, Remote Sensing Division, "Quick Look Images from the LEO-15 Experiment 2001," <http://rsd-www.nrl.navy.mil/7230/leo2001/LEO01QL.htm>.
9. W.J. Rhea, G. Lamela, and C.O. Davis, in preparation, 2004.
10. R. Steward and D. Kohler, Florida Environmental Research Institute, private communication.
11. P.N. Reinersman and K.L. Carder, "Monte Carlo Simulations of the Atmospheric Point-spread Function with an Application to Correction for the Adjacency Effect," *Appl. Opt.* **34**, 4453, 1995.
12. R. Lathrop, Director, Grant F. Walton Center for Remote Sensing and Spatial Analysis, <http://www.crssa.rutgers.edu/>
13. Terraserver.com, <http://terraserver.com/home.asp>
14. B.-C. Gao, M.J. Montes, Z. Ahmed, and C.O. Davis, "Atmospheric Correction Algorithm for Hyperspectral Remote Sensing of Ocean Color from Space," *Appl. Opt.* **39**, 887, 2000.

15. B.-C. Gao, M.J. Montes, and C.O. Davis, "New Algorithm for Atmospheric Correction of Hyperspectral Remote Sensing Data," *Proc. SPIE* **4383**, 23, 2001.
16. Z. Ahmad and R.S. Fraser, "An Iterative Radiative Transfer Code for Ocean-atmosphere Systems," *J. Atmos. Sci.* **39**, 656. 1994.
17. M.J. Montes and B.-C. Gao, "Tafkaa Users Guide," <http://rsd-www.nrl.navy.mil/7212/tafkaa.htm>.